

Improvements in Fixed-Valve Micropump Performance Through Shape Optimization of Valves

Adrian R. Gamboa
Christopher J. Morris
Fred K. Forster¹
e-mail: forster@u.washington.edu

Department of Mechanical Engineering,
Campus Box 352600,
University of Washington, Seattle, Washington
98195-2600

The fixed-geometry valve micropump is a seemingly simple device in which the interaction between mechanical, electrical, and fluidic components produces a maximum output near resonance. This type of pump offers advantages such as scalability, durability, and ease of fabrication in a variety of materials. Our past work focused on the development of a linear dynamic model for pump design based on maximizing resonance, while little has been done to improve valve shape. Here we present a method for optimizing valve shape using two-dimensional computational fluid dynamics in conjunction with an optimization procedure. A Tesla-type valve was optimized using a set of six independent, non-dimensional geometric design variables. The result was a 25% higher ratio of reverse to forward flow resistance (diodicity) averaged over the Reynolds number range $0 < Re \leq 2000$ compared to calculated values for an empirically designed, commonly used Tesla-type valve shape. The optimized shape was realized with no increase in forward flow resistance. A linear dynamic model, modified to include a number of effects that limit pump performance such as cavitation, was used to design pumps based on the new valve. Prototype plastic pumps were fabricated and tested. Steady-flow tests verified the predicted improvement in diodicity. More importantly, the modest increase in diodicity resulted in measured block-load pressure and no-load flow three times higher compared to an identical pump with non-optimized valves. The large performance increase observed demonstrated the importance of valve shape optimization in the overall design process for fixed-valve micropumps. [DOI: 10.1115/1.1891151]

1 Introduction

A variety of micropumps exist including those based on the combination of a deformable membrane, a piezoelectric bimorph actuator, and fixed geometry valves, i.e., "No Moving Parts Valves" (NMPV). Such valves develop a different pressure drop in the forward and reverse flow directions due to shape rather than mechanical moving parts. Orienting inlet and outlet valves in the preferential flow direction enables pumps based on these valves to generate net flow. Meso- and micro-scale pumps utilizing a variety of fix-valve configurations have been reported [1–3]. Some positive attributes of fixed-valve micropumps are simplicity of fabrication, versatility in pumping particle-laden fluids [4,5], and flexibility in designing for resonance, since the frequency of operation is not limited by mechanical valve dynamics.

The three primary steps of the design process investigated in this study with the goal of increasing the performance of NMPV micropumps are 1) optimizing valve shape, 2) predicting pump resonant behavior with a linear dynamic model, and 3) utilizing a system optimization technique based on the linear model to determine the best values for all geometric parameters, including valve size. The first step is entirely new and described in detail herein. The second step is accomplished by modeling the valves as straight channels of rectangular cross section, in which the fluid behavior is governed by the unsteady Navier-Stokes equations [6]. Step three, a systematic investigation of multiple design cases [7], was enhanced as part of this study by considering factors limiting performance, including available supply voltage, piezoelectric depolarization, and cavitation of the working fluid. In this study new techniques were used to fabricate plastic pumps, rather than

silicon-based devices reported in the past, which was part of an overall effort to design small scale phase-change cooling systems for electronics. The results presented consist of work previously reported in a proceedings paper [8] with comparisons of computational and experimental results.

To optimize valve shape, diodicity D_i was used as the basic measure of valve performance. This parameter is the ratio of the pressure drop in the reverse direction to that in the forward direction at a given steady-state volume flow rate,

$$D_i = \frac{\Delta p_r}{\Delta p_f} \quad (1)$$

The use of this steady flow measure of valve performance to improve the design of harmonically driven micropumps is a key hypothesis of this study. It is partially justified by previous studies of pump resonance based on the linear dynamic modeling with straight rectangular channels in the place of valves. Based on such modeling and experimental verification, maximum pump resonance typically occurs near the corner frequency of the valve fluid impedance curve [9], i.e., near a frequency, around which inertial effects are not dominant. In addition, the complexity of optimization based on transient analysis is so high, quasi-steady optimization was investigated to determine its value. Furthermore, even though fluid inertia has a first-order effect on pump resonance, because its effect is typically greater than that due to the mass of the pump membrane [6], the directional flow behavior of the valves is assumed quasi-steady, similar to that of an electrical diode for which inductance is neglected.

In this paper shape optimization of Tesla-type valves first described by Tesla [10] and first utilized in a micropump by Forster et al. [3] is presented. The basic procedure used is applicable to any parametrically described valve shape, such as the simple diffuser [2,11], nozzle-diffuser¹², filleted diffuser¹³, and tesser valve¹⁴.

¹Corresponding author

Contributed by the Fluids Engineering Division for publication in the JOURNAL OF FLUIDS ENGINEERING. Manuscript received by the Fluids Engineering Division November 3, 2002. Revised manuscript received December 5, 2004. Review conducted by K. Breuer.

2 Methods

The methods utilized in this study are presented in four parts. First, valve shape optimization using commercial computational fluid dynamic (CFD) software is described. Valve sizing is then described based on a linear model of pump resonance. Plastic pump fabrication methods used to manufacture prototypes are then described. Lastly, testing methods are described that were used to examine how valve shape affected pump performance.

2.1 Valve Fluid Dynamics. The FLOTRAN component of ANSYS version 6.1 (ANSYS, Inc., Canonsburg, PA) was utilized to calculate velocity and pressure throughout the Tesla-type valve. Optimization of valve shape to maximize diodicity was accomplished through the use of a parametric description of the Tesla-type valve based on six geometric design variables. Optimization was performed to determine the best set of these design variables with the ANSYS Subproblem Approximation method that utilized the results of the flow field calculations for each set of design variables considered.

2.2 Flow Field Calculations. Solutions of the Navier–Stokes equations were confined to two-dimensional, incompressible, and steady-state laminar flow. By solving these equations in non-dimensional form, a universal solution was obtained for any size valve of a particular shape that depended only on Reynolds number. The dimensionless quantities used were

$$\tilde{\mathbf{u}} \equiv \frac{\mathbf{u}}{2U}, \quad \tilde{p} \equiv \frac{p}{\rho(2U)^2}, \quad \tilde{\mathbf{r}} \equiv \frac{\mathbf{r}}{L}, \quad (2)$$

where U is the characteristic velocity, and L is the characteristic length. For the Tesla-type valve U was chosen as the mean flow velocity in the inlet channel and L was the channel width w_v . The dimensionless form of the incompressible steady-state Navier–Stokes equations is then

$$\tilde{\mathbf{u}} \cdot \tilde{\nabla} \tilde{\mathbf{u}} = -\tilde{\nabla} \tilde{p} + \frac{1}{\text{Re}} \tilde{\nabla}^2 \tilde{\mathbf{u}}, \quad \text{Re} = \frac{2\rho UL}{\mu} = \frac{\rho U D_h}{\mu}, \quad (3)$$

where the dimensionless operator $\tilde{\nabla} \equiv L\nabla$ and $D_h = 2w_v$ is the hydraulic diameter. To simplify the assignment of Re in the non-dimensional computations, for which valve width is unity, i.e., $D_h = 2$, velocity and density were chosen such that $U = 1/2$ and $\rho = 1$. With these assignments, the fluid dynamic viscosity in the CFD model was assigned the value

$$\mu_{\text{CFD}} = 1/\text{Re}. \quad (4)$$

The computational grid was designed to adapt to changes in geometry and maintain sufficient grid densities in areas of large velocity and pressure gradients. This was done by carefully biasing element size. To speed solution time unnecessary elements were reduced by using coarse grids in appropriate areas and reducing elements in the streamwise direction along long channel lengths. Rectangular elements were used, with 16 elements across each valve channel resulting in 7000 to 10 000 total elements. Grid independence was checked by doubling the number of elements and determining that the solution changed less than 4%.

Inlet and outlet boundary conditions were applied to the straight walls of plenums, which were used to model actual plenums and pump chambers (see Fig. 1). The inlet condition was uniform velocity, and the outlet condition was zero pressure. Finally, the no-slip velocity condition was applied to valve walls and the curved walls of the plenums.

Solution options were chosen based on accuracy, stability, and execution time. The velocity and pressure were calculated using the semi-direct solvers Conjugate Residual (CR) and the Pre-Conditioned Conjugate Residual (PCCR) methods, respectively. Solver relaxation was fine-tuned to decrease solution time while maintaining solution accuracy. Coupling between the momentum and pressure equations was handled by an enhanced Semi-Implicit Method for Pressure Linked Equations (SIMPLE) algorithm, the

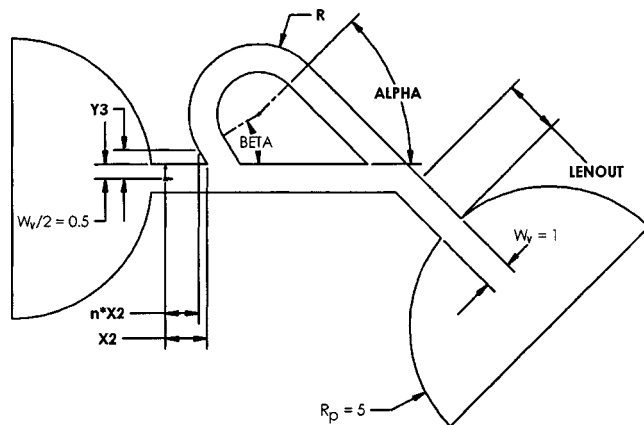


Fig. 1 Design variables for the Tesla-type valve: 1) the length of the inlet segment in forward flow X_2 , 2) scale factor n yielding the coordinate nX_2 , and 3) coordinate Y_3 that defined the outer tangent location of the return section of the loop segment, 4) loop outer radius R , 5) outlet segment length LENOUT , and (6) outlet segment angle α . The origin of coordinates is on the centerline of the inlet channel, one-half channel width from its left end.

SIMPLEN method. The advection scheme for the momentum equation used the second-order accurate Streamline Upwind/Petrov-Galerkin (SUPG) method while the pressure equation used the first-order accurate Monotone Streamline Upwind (MSU) method.

Convergence was controlled with a convergence monitor for each degree of freedom (DOF). The convergence monitor was based on a calculation of the sum of changes in DOF between the current iteration and previous iteration divided by the sum of the current DOF. The convergence monitors were relaxed by one order of magnitude from default values to 10^{-1} for velocity DOFs and to 10^{-7} for pressure.

Flow field calculations were performed on a cluster of ten IBM RS/6000 computers running the AIX operating system. Thirteen values of Reynolds number over the range $0 < \text{Re} \leq 2000$ were considered, and at each value calculations were performed in both the forward and reverse flow direction for each valve shape considered.

2.3 Shape Optimization. To optimize valve shape based on solutions for the flow field, valve geometry was described with six independent non-dimensional design variables as shown in Fig. 1. Since the non-dimensionalization was based on valve channel width, that parameter was unity and therefore not one of the design variables. Special attention was paid to the loop return region, which consisted of a straight channel segment oriented at the angle β . This angle was not one of the design variables but was based on the coordinates nX_2 and Y_3 . Describing the flow loop in this manner avoided interference with the plenum and yielded a wider range of β than was possible with the parametric model previously investigated¹⁵. For comparison a second valve was modeled based on an empirically designed, commonly used valve reported previously [6], and referred to as a Tesla-type I valve in that study and here simply referred to as the reference valve. It differed slightly from the Tesla-type I valve, for which the constant radius flow loop intersects the main channel at a right angle. The reference valve flow loop return segments intersected the main channel at approximately nine degrees from perpendicular.

To maximize valve diodicity an object function to be maximized was based on the integral over Reynolds number of the product Di and a weighting function,

$$\int_{\text{Re}_{\min}}^{\text{Re}_{\max}} \frac{Di}{(\Delta\tilde{p}_r)^m} d\text{Re}, \quad (5)$$

where in this study $\text{Re}_{\min}=0$, $\text{Re}_{\max}=2000$, and $m=1$. The weighting function chosen was used to control valve resistance while maximizing diodicity. The values of $\Delta\tilde{p}_r$ and $\Delta\tilde{p}_r$ in Eq. (5) were determined from the calculated pressure at the midpoint of the centerline of each plenum shown in Fig. 1. This location was not critical because pressure was relatively uniform over much of each plenum.

2.4 Valve Sizing. Valve size was determined by examining multiple pump designs with a previously reported linear model of pump resonance [6], which was in the form of code written in MATLAB (version 6.5, The Mathworks, Inc, Natick, MA). Starting with a particular pump chamber diameter, optimization of other pump parameters was mainly directed toward determining the best combination of actuator geometry (cover plate thickness and piezoelectric element radius and thickness) and valve size. This approach was based on the fact that pump resonance is primarily determined by driving element stiffness and inertance of the fluid in the valves.

For this study the existing linear model was extended to include important voltage-limiting effects. First, cavitation often limits maximum pump performance. In addition, the voltage applied to the piezoelectric element must not cause the electrical field across it to exceed the depolarization level E_{depol} . Lastly, $V_{s,\text{max}}$ is the maximum (zero-to-peak) voltage amplitude generated by the supply amplifier. Based on static cavitation pressure P_{cav} in the pump chamber, the maximum possible (or cutoff) voltage $V_{s,c}$ that can be applied is

$$V_{s,c} = \min \left[\frac{P_{cm} - P_{\text{cav}}}{P_c}, E_{\text{depol}} t_p, V_{s,\text{max}} \right], \quad (6)$$

where P_c is the harmonic amplitude of the pump chamber pressure per volt about the time-averaged mean chamber pressure P_{cm} , and t_p is the piezoelectric element thickness. Since P_c is a function of frequency, so is $V_{s,c}$. It follows that the outlet valve volume flow rate harmonic amplitude, like any other model output variable, also has a frequency-dependent cutoff value

$$Q_{0,c} = V_{s,c} Q_0, \quad (7)$$

where Q_0 is harmonic amplitude of the outlet valve volume flow rate per volt.

The effect of reduced static pressure in the valves due to fluid velocity was also taken into account by replacing the voltage limit due to static cavitation in Eq. (6) with the solution for V_s in the relation

$$V_s P_c = P_{cm} - \frac{1}{2} \rho (Q_0 V_s / A_v)^2 - P_{\text{cav}}, \quad (8)$$

where A_v is the cross-sectional area of the valve channels, and where it is assumed the inlet and outlet valves are identical. The result is given by

$$V_{s,c} = \min \left[\dots \frac{A_v^2 P_c}{\rho Q_0^2} \left(\sqrt{1 + \frac{2\rho Q_0^2}{A_v^2 P_c^2} (P_{cm} - P_{\text{cav}}) - 1} \right), E_{\text{depol}} t_p, V_{s,\text{max}} \right]. \quad (9)$$

For purpose of calculation, Eq. (9) may be an inappropriate form when the dynamic pressure effect approaches zero, which is equivalent to ρ approaching zero. Taking the limit of this expression as $\rho \rightarrow 0$ and using a binomial expansion for the radical, Eq. (9) reduces to Eq. (6) to order ρ^2 . Thus the two expressions can be combined based on the value of

Table 1 Geometric parameters for fabricated pumps. Additional parameters common to all pumps are described in the text.

Pump ID	Tesla valve type	Valve width w_v (μm)	Valve aspect ratio d_v/w_v	Normalized valve length L_v/w_v	Memb. thick. (μm)
p28	opt	135	2.78	15.5	460
p29	opt	500	2.42	15.5	460
p30	ref	300	2.50	16.7	270
p31	opt	300	2.50	15.5	270

$$\epsilon = \frac{\rho Q_0^2}{A_v^2 P_c} \frac{P_{cm} - P_{\text{cav}}}{P_c}, \quad (10)$$

or

$$V_{s,c} = \begin{cases} \text{Eq. (6)} & \text{if } \epsilon < \epsilon_0 \\ \text{Eq. (9)} & \text{otherwise,} \end{cases} \quad (11)$$

where ϵ_0 is the smallest number that can be differentiated from unity. Using MATLAB on a Pentium III PC $\epsilon_0 \approx 2 \times 10^{-16}$.

With the above performance-limiting effects considered, the linear system model was used to investigate a wide range of membrane thicknesses and valve sizes. As in [6], the electro-mechanical parameters of the piezoelectrically driven membrane were calculated with finite element analysis, and these values were utilized for the linear system model. A three-dimensional model was used to capture the effects of the non-axisymmetric piezoelectric actuator used (see the next section). The valve equivalent lengths, or the straight channel lengths used to represent the valves, were calculated based on an average path between the forward and reverse directions through the valve, as in [6]. Based on the results of the linear model, several pumps were fabricated.

2.5 Pump Fabrication. Pumps with 10-mm-diam chambers were fabricated by conventional machining techniques using 125 μm and larger end mills (Kemmer Präzision) and a miniature milling machine (Model 5410, Sherline Products Inc., Vista, CA) modified for computer numerical control (CNC) (Model 999-6100-005, MicroKinetics Corp., Kennesaw, GA). This allowed rapid progression from CAD design to prototype compared to silicon-based micro-fabrication.

Pump chamber and valves were machined in acrylic to equal depths. Polycarbonate membranes were bonded to the housings using a cyanoacrylate adhesive (Loctite 420 Superbond). Piezoelectric wafers 9 mm in diameter and 127 μm thick (PZT-5A, Piezosystems, Cambridge, MA) were bonded to the membranes using the same adhesive. Electrical connections were made to a 1.5-mm-wide "tab" on the piezoelectric driver that extended 2.5 mm beyond the pump chamber. A small pocket was cut through the membrane and into the pump housing below this tab to allow for electrical lead clearance. The pump inlets and outlets were made by gluing 2.08 mm inside diameter stainless steel tubes with a rapid-cure epoxy. Table 1 gives the different geometric parameters for the four pumps constructed and tested in this study. Note that pumps 30 and 31 only differ with respect to valve type.

2.6 Pump Experiments. For comparison with CFD results, diodicity versus Reynolds number for pumps 30 and 31 were measured. For each value of Re , a syringe pump (Model 200, KD Scientific, Boston, MA) delivered steady flow, and pressure drop was measured with a water column for pressures below 5 kPa, and a pressure transducer (EPI-127, Entran Sensors & Electronics, Fairfield, NJ) for pressures above that value. The resulting pressure drop was divided by two to arrive at Δp across a single valve, assuming each valve experienced the same entry and exit effects

Table 2 Optimized and reference Tesla-type valve parameters. Linear dimensions are normalized by channel width.

Valve	X_2	n	Y_3	LENOUT	R	α	β	Average Di
Optimized	1.60	0.797	0.608	2.94	2.35	41.9°	71.7°	1.50
Reference	1.50	0.990	0.600	2.00	2.50	45.0°	8.53°	1.21

and negligible pressure drop through the pump chamber. Finally, Di was calculated from measured values for Δp_r and Δp_f according to Eq. (1).

Linear model predictions of membrane velocity resonance were compared to experimental data by measuring the resonance behavior of each pump. First isopropanol alcohol was used for priming. Then each pump was filled by flushing with 10 ml of de-ionized water that had been degassed by boiling for 10 min and cooled to room temperature. Tubes used for filling were disconnected so that menisci of water were visible at the ends of the stainless steel inlet/outlet tubes. The membrane centerline velocity was measured using a laser vibrometer (Model OVF 302, Polytec, Waldbronn Germany), while a signal generator (Model 19, Wavetek, United Kingdom) applied a harmonic input voltage to the pump actuator through an amplifier (EPA-102, Piezosystems Inc., Cambridge, MA).

Finally, to compare pump performance, measurements were made for each pump at two outlet static pressure loads: blocked-flow, i.e., the pressure at which net flow ceased, and no-load flow, both with the inlet held at atmospheric pressure. For blocked-flow the pressure was measured with the pressure transducer, which was connected to the pump outlet with a 5-cm-long piece of tubing having a compliance of approximately $0.0015 \text{ mm}^3/\text{Pa}$. Flow rate at zero pressure was measured by inserting the pump inlet tube into a petri dish filled with degassed water, and allowing the outlet tube to discharge to another petri dish on an electronic scale (1205 MP, Sartorius, Westbury, NY) at the same hydrostatic pressure. The time for a change in mass of at least 250 mg to occur was recorded, and the flow rate was calculated using the density of water (taken as 1000 kg/m^3). Performance measurements for a particular supply voltage were made at the highest frequency attained, which corresponded to the frequency at which either cavitation or resonance occurred. The ambient temperature for all tests was $26 \pm 1 \text{ }^\circ\text{C}$.

3 Results and Discussion

3.1 Valve Shape Optimization. The optimization calculations required consideration of up to 40 different sets of design variables. Approximately 1000 separate flow field calculations were performed, each taking from 3000 to 8000 cpu-seconds depending on valve shape. The resulting optimized design variables along with the reference valve geometry are shown in Table 2, and the corresponding shapes in graphic form are shown in Fig. 2. The return angle β (determined by the design variables X_2 , Y_3 , and n) was found to be substantially larger for the optimized valve. Vector plots of the velocity in the loop return region of these valves shown in Figs. 3 and 4 reveal that by increasing β , flow in the loop section is directed to oppose flow in the main channel. This suggests that the losses generated by introducing the fluid with a velocity component opposite to the pressure gradient in the main channel may be important for maximizing diodicity. While this may seem obvious, it should be noted that if this observation is correct, other details of the loop geometry need to be such that significant flow occurs in the loop during the reverse flow period. More work is necessary to understand this more fully, as the optimized Tesla-type valve appears to be a subtle balance of channel lengths and orientations.

Figure 5 shows the CFD results for Δp_r and Δp_f dimensionalized for the size of the valves used in pumps p30 and p31 in accordance with Eq. (2) and properties of water at $25 \text{ }^\circ\text{C}$. The

optimized valve was found to have a significant increase in Δp_r with little difference in Δp_f compared to the reference valve. For the optimized valve Δp_r was over 30% higher for $1000 < \text{Re} < 2000$, while Δp_f was consistently within 1–2% of the reference valve values. This behavior may be the result of the weighting function used in the object function Eq. (5), incorporated to minimize losses in the forward direction. Thus, the weighting function chosen was successful in controlling a specific fluid dynamic characteristic while diodicity was optimized.

The experimental results for forward and reverse steady flow pressure drop are shown in Fig. 6 for devices p30 and p31. The qualitative agreement with the calculated values shown in Fig. 5 is good. And, as was seen with the CFD calculations, the optimized valves showed a significant increase in Δp_r with little difference in Δp_f compared to the reference valve.

The graph of diodicity versus Reynolds number for the optimized and reference valves is shown in Fig. 7. Calculated diodic-

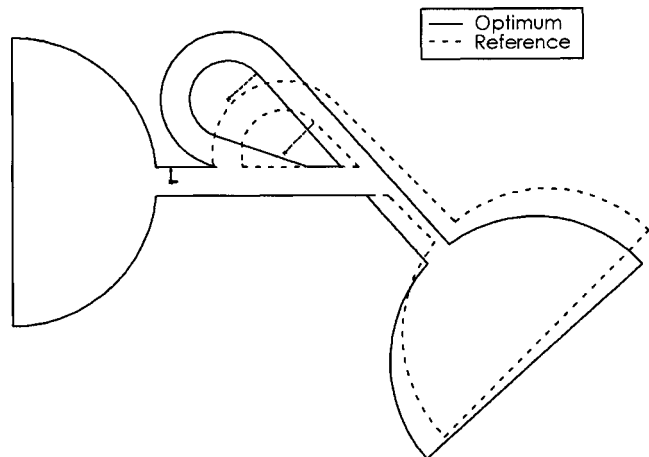


Fig. 2 Optimized and reference Tesla-type valve

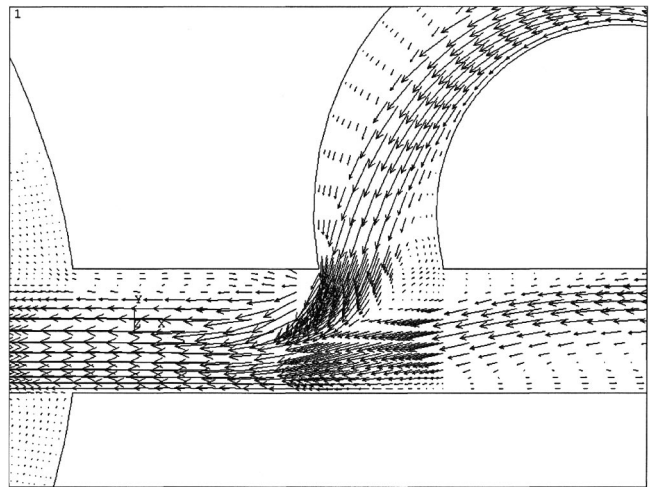


Fig. 3 Vector plot of the velocity in the flow loop return region of the reference valve

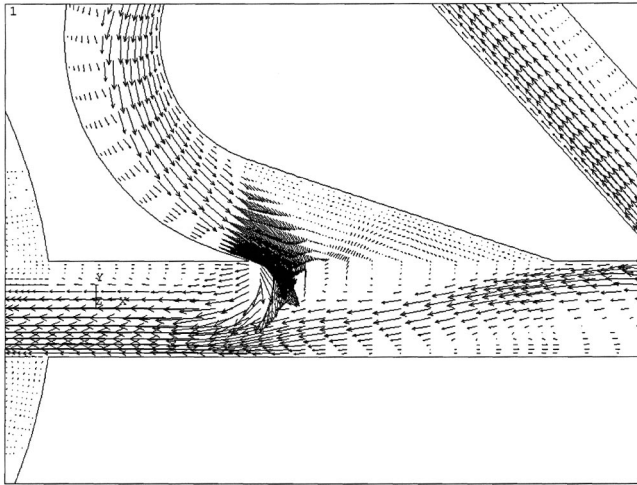


Fig. 4 Vector plot of the velocity in the flow loop return region of the optimized valve

ity increased by a maximum of 37% at $Re=2000$ and by an average of 25% over the range $0 < Re < 2000$, and similar results are apparent from the experimental data. However, while the degree of improvement is quite similar for both calculated and measured results, there are distinct differences in the shape of the curves. The measured values for the optimized valve are significantly higher than those calculated for $Re < 500$, and a similar behavior may exist for the reference valve. In addition, the measured diodicity for the reference valve does not monotonically increase, a behavior seen in all three of the other curves.

The primary reason for differences between calculated and measured diodicity is most likely related to the limitations of the two-dimensional (2-D) modeling. A physical argument for the 2-D calculations predicting higher diodicity than measured is that loss mechanisms in the Tesla-type valve may be primarily due to out-of-plane vorticity, which may be overestimated in the 2-D model. However, this cannot explain the behavior at lower Reynolds number. Additional three-dimensional (3-D) modeling is necessary to understand these differences more fully. Nevertheless, the results shown in Fig. 7 demonstrate the ability of 2-D modeling to improve valve performance.

It should be noted that in this study the Reynolds number range was $0 < Re < 2000$. However, depending on pump chamber size

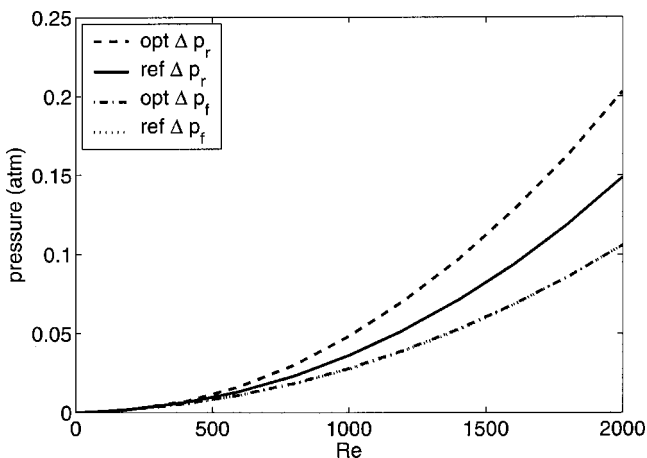


Fig. 5 Calculated reverse and forward pressure drop for the optimized (opt) and reference (ref) Tesla-type valves, based on 2-D CFD results for $w_v=300 \mu m$ and water at $25^\circ C$. Note the curves for forward flow are nearly identical.

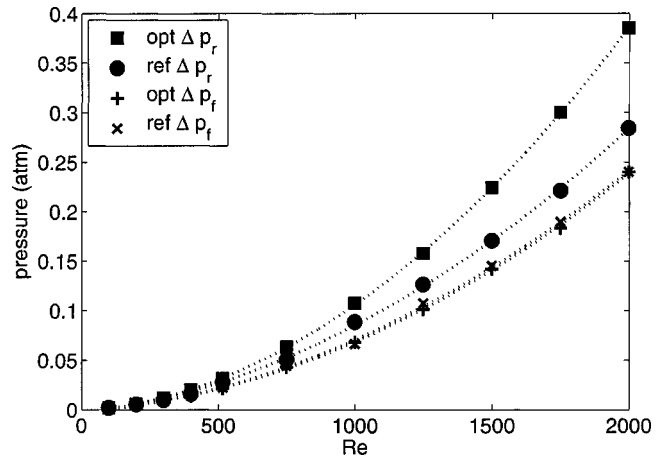


Fig. 6 Measured reverse and forward pressure drop for the optimized (opt) and reference (ref) Tesla-type valves, for devices p30 and p31 and water at $25^\circ C$. The dotted curves are second-order polynomials fit to the data for use in estimating diodicity versus Reynolds number

and expected flow rates, the range of Re considered for shape optimization could be matched to actual values through an iterative process. This may be a fruitful approach since the shape optimization process could yield different results depending on the range considered.

3.2 Valve Sizing. The linear pump model based on reduced-order parameters allowed for the consideration of multiple design cases and revealed many interesting results about valve size in terms of the amplitude of various harmonic output parameters per unit input voltage and at maximum possible input voltage. Figure 8 shows the membrane velocity amplitude per unit input voltage versus valve width and membrane thickness for a 10-mm-diam polycarbonate membrane, with a 2.5 valve depth-to-width aspect ratio, a chamber depth equal to the valve depth, and a length-to-width ratio of 16, a value between that of the optimized and reference valve (see Table 1). The results in Fig. 8 ignore the voltage limitation effects. Larger membrane thickness yields larger membrane velocities for a given valve size. This is consistent with past findings on the importance of stiff membranes [10]. In addition, larger valve size for a given membrane thickness also yields higher membrane velocity due to lower valve resistance. All other

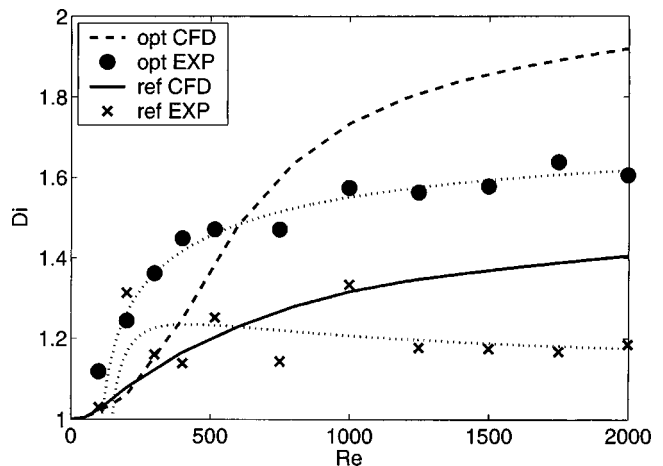


Fig. 7 Comparisons of calculated (CFD) and measured (EXP) Di versus Re for the optimized (opt) and reference (ref) Tesla-type valves. The dotted curves are calculated diodicity based on the polynomials fit to the data shown in Fig. 6.

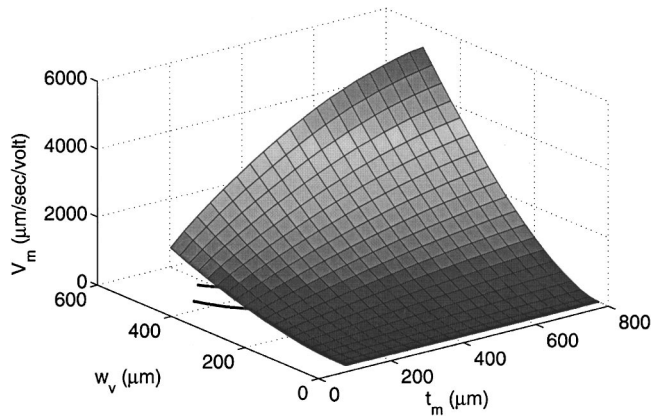


Fig. 8 Membrane velocity harmonic amplitude V_m versus valve width w_v and polycarbonate membrane thickness t_m for a 10-mm-diam pump with a 2.5 valve depth-to-width aspect ratio, a chamber depth equal to the valve depth, and a valve length-to-width ratio of 16. The piezoelectric element size was held constant at 9 mm in diameter and 127 μm thick. Each point on the surface corresponds, in general, to a different driving frequency.

model output parameters followed these two trends of higher values with thicker membranes and larger valves when considered on a per unit voltage basis.

Significantly different design surfaces resulted when the voltage was limited according to Eq. (11). This is seen in Fig. 9, which shows membrane velocity harmonic amplitude corresponding to the maximum input voltage possible, which in general is different at each design point. Figure 10 shows the corresponding chamber pressure harmonic amplitude, which exhibits a large “shelf” across much of the design space at a value of approximately 1 atm. This indicates that pumps built within that region are predicted to have cavitation as the limiting factor and that the response surfaces for all output parameters in that region will be affected. In the case of membrane velocity the peak value occurred at the edge of the “shelf” where valve size was large and membrane thickness was low, whereas without voltage limitations considered it occurred at large valve size and large membrane thickness.

Figure 11 shows the voltage-limited harmonic amplitude of valve Reynolds number as a function of valve width and mem-

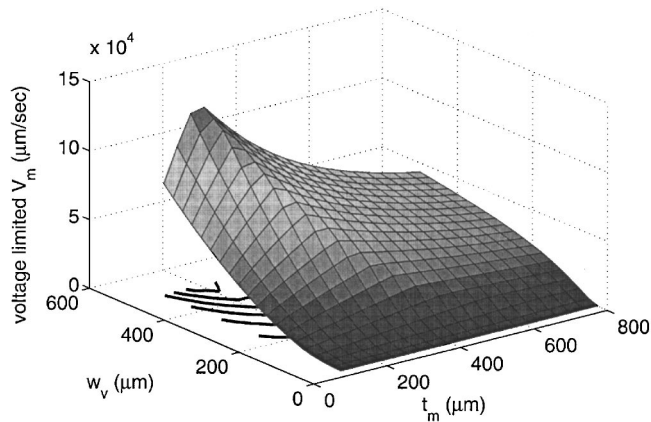


Fig. 9 Voltage-limited membrane velocity harmonic amplitude versus valve width and polycarbonate membrane thickness for the same combination of parameters as in Fig. 8. The voltage limits account for a 180 V supply maximum, a depoling electric field of 5×10^5 V/m, and a cavitation pressure equal to vapor pressure at 25 °C.

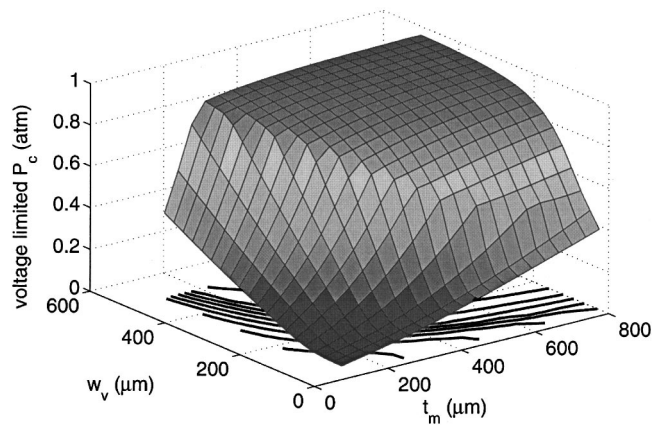


Fig. 10 Voltage-limited chamber pressure harmonic amplitude versus valve width and polycarbonate membrane thickness for the same combination of parameters as in Fig. 8. The voltage limits were accounted for in the same way as in Fig. 9.

brane thickness. This parameter was derived from the voltage-limited valve flow rate harmonic amplitude according to the expression $Re = \rho Q_0 D_h / A_v \mu$. It should be an important parameter on which to optimize net pump performance in terms of net flow and net pressure, given that the results from CFD calculations and experiment show higher diodicity with increasing Reynolds number as shown in Fig. 7. The maximum value of Reynolds number harmonic amplitude shown in Fig. 11 occurs in the region of larger valve size and smaller membrane thickness. It is reasonable to expect the maximum value in this region, because the lower flow restriction of larger valves allows the volume flow rate induced by the membrane motion to be translated into valve flow rather than compression of compliance elements, such as gas in the working fluid, and the lower flow resistance results in less system damping and consequently higher resonant amplitudes. However, eventually the valves become so large that the resonant amplitude of membrane motion and the ensuing valve flow rate falls due, in part, to the lower inertance of larger valves that plays an important role in system resonance. Additionally, Reynolds number is inversely proportional to valve size for the same flow rate. Thus, sizing valves for maximum Reynolds number alone should lead to good net flow rate performance but only at low net pressure head.

The above-described situation is reversed for stiffer membrane

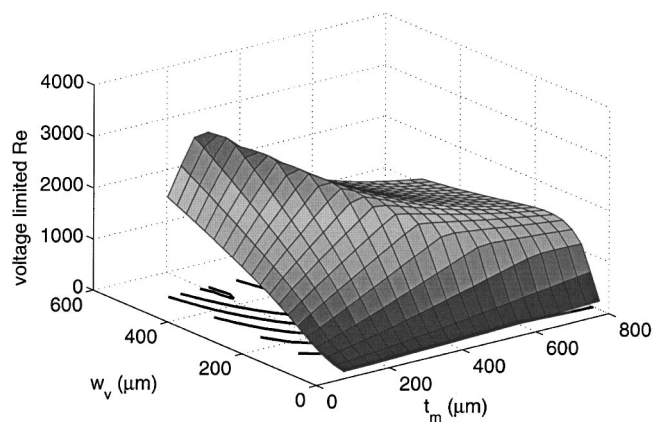


Fig. 11 Voltage-limited valve Re harmonic amplitude versus valve width and polycarbonate membrane thickness for the same combination of parameters as in Fig. 8. The voltage limits were accounted for in the same way as in Fig. 9. The maximum is near $[t_m, w_v] = [400, 200]$ μm .



Fig. 12 A 10 mm pump chamber with 300- μm -wide optimized Tesla valves from Table 2. The pump body is acrylic, and a PZT-5A actuator is bonded to a 270- μm -thick polycarbonate membrane. The electronic computer chip indicates its intended application.

and smaller valve size, which are expected to generate a lower net flow but higher net pressure at the same cavitation-limited chamber pressure amplitude. From Fig. 11 it is seen that the maximum Reynolds number for any valve size occurs along a ridge that runs from large valve size and small membrane thickness to small valve size and large membrane thickness, which corresponds to the boundary of the cavitation region shown in Fig. 10. Thus, from the results of the linear system model, it is expected that the nonlinear effect of valve diodicity for combinations of valve size and membrane stiffness that lie along the ridge will result in pump performance in terms of high no load flow, high block load pressure or optimal combinations of these two extremes. In other words, utilizing the ridge may allow customizing net pressure versus net flow performance for particular applications. Because of the potential for optimal pumps in this sense, pumps were built with different membrane thickness and valve size to investigate combinations of valve size and membrane thickness between the opposite corners of the design space.

3.3 Pump Resonance and Performance. The four pumps in this study were chosen to have a variety of parameter combinations. Figure 12 shows the pump identified as p31. This pump, as well as each pump from Table 1, was tested at both low voltage for resonant behavior and at high voltage for pump performance. The measured resonant behavior at low voltage is shown in Fig. 13 where it can be seen that good agreement was obtained for the model predictions of membrane velocity for each of the design parameter combinations. The disagreement in predicted frequency for devices p30 and p31 was well within reason considering that model predictions were made entirely based on first principles [6]. It is also seen that pumps p30 and p31 had very similar linear behavior when viewed as pairs of model predictions or measured results. This was apparently the result of the fact that their different shapes caused only a small difference in average path length-to-width ratio, 15.5 for the optimized valve and 16.7 for the reference valve.

The measured high-voltage pump behavior is shown in terms of pump performance Fig. 14. Conclusions may be drawn about the three pumps with the same valve shape but with different valve

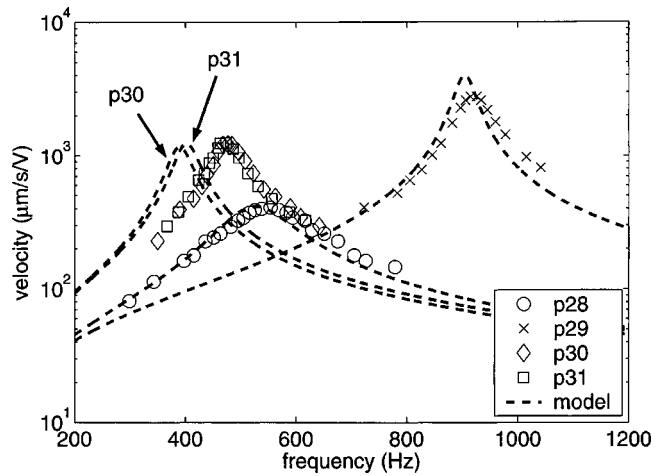


Fig. 13 Measured membrane centerline velocity-per-volt (symbols) compared with model predictions (---) for all pumps in Table 1. Actuation voltage for the measurements was approximately 3 V peak-to-peak.

sizes and membrane thicknesses. The behavior of pump p28 relative to pump p29 indicates that the former did better in net pressure but poorer in net flow, consistent with the argument presented in the previous section. It was somewhat surprising that p31 produced a performance curve that equaled the block load pressure of p28 while producing significantly better no load flow. This may be an indication that pumps corresponding to the ridge of the Re surface in Fig. 11 represent good designs, but the trade-off between pressure and flow performance is not completely understood. Future work should aim to accurately quantify the predictions of net flow and pressure from the linear model, so that a pump may be more accurately designed for desired performance in terms of both pressure and flow.

Most notable of the results shown in Fig. 14 is the comparison between pumps p30 and p31. Pump p31 was nearly identical to p30 in terms of the linear model parameters characterizing it as demonstrated in Fig. 13. Yet pump p31 with shape optimized valves is seen to have nearly three times the performance of pump p30 at approximately the same driving level in terms of both pressure and flow developed. This result is qualitatively consistent

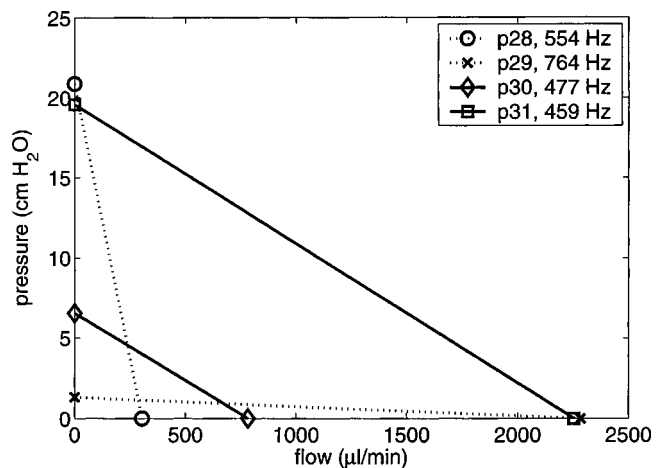


Fig. 14 Measured pressure-flow pump performance curves for the pumps shown in Table 1 at approximately 120 V peak-to-peak and the highest frequency at which each pump successfully operated. Lines are drawn between points for clarity. The performance enhancement between p30 and p31, made possible by valve shape optimization, is clearly shown.

with even the simplest models relating net flow to diodicity, which show that for values of diodicity less than two, small improvements in diodicity lead to relatively large improvements in net flow rate ([3], Fig. 1). The fact that the improvement was so large could be due to effects caused by unsteady flow that were not included in the quasi-steady valve flow calculations. Nevertheless, the measured improvement validates the approach used in this study to determine *how* to achieve higher diodicity for improved pump performance.

4 Conclusions

A design process for optimizing fixed-geometry valve shape and size was accomplished. Optimization of valve shape using CFD that incorporated automatic search methods was demonstrated on a Tesla-type valve with a significant increase in calculated diodicity compared to a commonly used reference valve over the range Reynolds number $0 < Re \leq 2000$. The calculated results compared favorably with experiment. A linear system model was used to determine valve size and membrane thickness for best pump performance. Pump fabrication techniques utilizing CNC machining of acrylic plastic were introduced as a rapid micropump prototyping technique. Measurements made on the fabricated pumps showed that net pressure and flow for a pump with optimized valve shape was nearly three times larger than that for an identical pump but with valves of non-optimized shape.

This study also demonstrated the value of the linear model used in that it was originally developed for silicon/Pyrex fabrication, but was used successfully in this study for designs in acrylic/polycarbonate, which have significantly different material properties. And the basic simplicity of fabrication for NMPV pumps was demonstrated by the ease with which we were able to fabricate pumps using new materials.

Acknowledgments

This work was supported in part by a subcontract from NASA Goddard Space Flight Center contract NASS-03059 awarded to MicroEnergy Technologies Inc., Washington Technology Center Research Technology Development Agreement WTC FTI 03-10, a fellowship from the University of Washington Graduate Opportunities & Minority Achievement Program, and a grant from the Hispanic Scholarship Fund.

Nomenclature

A_v	= valve cross-sectional area (m ²)
D_h	= valve hydraulic diameter $2(w_v d_v)/(w_v + d_v)$ (m)
Di	= steady-state valve diodicity $\Delta p_r/\Delta p_f$
d_v	= valve depth (m)
E_{depol}	= piezoelectric depolarization limit $[5 \times 10^5 \text{ V/m}]$
L_v	= valve length (m)
LENOUT	= valve outlet segment length (m)
n	= nX_2 is a coordinate location for the valve loop straight segment (see Fig. 1)
p	= pressure (Pa)
P_c	= amplitude of harmonic chamber pressure about P_{cm} (Pa)
P_{cm}	= temporal mean (dc) chamber pressure (Pa)
Q_0	= amplitude of harmonic volume flow rate through outlet valve (m ³ /s)
\mathbf{r}	= position vector (m)
R	= valve loop segment outer radius (m)

R_p	= plenum radius (m)
Re	= valve Reynolds number $\rho U D_h/\mu$
t_m	= cover plate (membrane) thickness (m)
t_p	= piezoelectric element thickness (m)
u	= velocity (m/s)
U	= valve characteristic velocity (m/s)
V_m	= amplitude of harmonic velocity of membrane centerline velocity (m/s)
V_s	= supply voltage (V)
w_v	= valve width (m)
X_2	= valve inlet segment length (m)
Y_3	= a coordinate location for the valve loop straight segment (see Fig. 1) (m)
α	= valve outlet segment angle
β	= valve loop return segment angle
μ	= absolute viscosity (Pa s)
μ_{CFD}	= CFD model viscosity (Pa s)
ρ	= density (kg/m ³)
$(\bar{\quad})$	= non-dimensional quantity
$(\quad)_f$	= forward direction
$(\quad)_r$	= reverse direction

References

- [1] Stemme, E., and Stemme, G., 1993, "A valveless diffuser/nozzle-based fluid pump," *Sens. Actuators, A*, **39**, pp. 159–167.
- [2] Gerlach, T., and Wurmus, H., 1995, "Working principle and performance of the dynamic micropump," *Sens. Actuators, A*, **50**, pp. 135–140.
- [3] Forster, F., Bardell, R., Afromowitz, M., and Sharma, N., 1995, "Design, fabrication and testing of fixed-valve micropumps," in *Proceedings of the ASME Fluids Engineering Division 1995*, San Francisco, D. C. Wiggert et al. (Eds.), ASME, Vol. FED-234, pp. 39–44.
- [4] Jang, L.-S., Morris, C. J., Sharma, N. R., Bardell, R. L., and Forster, F. K., 1999, "Transport of particle-laden fluids through fixed-valve micropumps," in *Micro-Electro-Mechanical Systems (MEMS)*, 1999 ASME International Mechanical Engineering Congress and Exposition, A. P. Lee et al. (Eds.), Vol. MEMS-1, pp. 503–509.
- [5] Jang, L.-S., Sharma, N. R., and Forster, F. K., 2000, "The effect of particles on the performance of fixed-valve micropumps," in *Micro Total Analysis Systems 2000*, A. van den Berg, W. Olthuis, and P. Bergveld (Eds.), pp. 283–286.
- [6] Morris, C. J., and Forster, F. K., 2003, "Low-order modeling of resonance for fixed-valve micropumps based on first principles," *J. Microelectromech. Syst.*, **12**(3), pp. 325–334.
- [7] Williams, B. E., and Forster, F. K., 2001, "Micropump design for optimum pressure/flow characteristics," in *Micro-Electro-Mechanical Systems (MEMS)*, ASME International Mechanical Engineering Congress and Exposition, A. P. Lee (Ed.), ASME, Vol. MEMS-3, pp. 647–655.
- [8] Gamboa, A. R., Morris, C. J., and Forster, F. K., 2003, "Optimized fixed-geometry valves for laminar flow micropumps," in *Proceedings of the ASME Fluids Engineering Division 2003* (Washington, DC), Vol. FED-259, pp. 525–534.
- [9] Morris, C. J., and Forster, F. K., 2004, "Oscillatory flow in microchannels: Comparison of exact and approximate impedance models with experiment," *Exp. Fluids*, **36**(6), pp. 928–937.
- [10] Tesla, N., 1920, "Valvular Conduit," U.S. Patent No. 1,329,559.
- [11] Groisman, A., and Quake, S. R., 2004, "A Microfluidic Rectifier: Anisotropic Flow Resistance at Low Reynolds Numbers," *Phys. Rev. Lett.*, **92**(9), pp. 094501.
- [12] Olsson, A., Enoksson, P., Stemme, G., and Stemme, E., 1995, "A Valve-less Planar Pump in Silicon," in *Transducers '95* (Stockholm), Vol. 2, pp. 291–294.
- [13] Olsson, A., Stemme, G., and Stemme, E., 1999, "Numerical Simulations of Flat-Walled Diffuser Elements for Valveless Micropumps," in *Proceedings of the Microsystems Modeling Conference*, pp. 585–588.
- [14] Forster, F. K., and Williams, B. E., 2002, "Parametric design of fixed-geometry microvalves—the Tesser valve," in *Proceedings of the ASME Fluids Engineering Division*, International Mechanical Engineering Congress and Exposition, A. Ogut (Ed.), ASME, Vol. FED-258, pp. 431–437.
- [15] Bardell, R., Sharma, R., Forster, F. K., Afromowitz, M. A., and Penney, R., 1997, "Designing high-performance micro-pumps based on no-moving-parts valves," in *Micro-Electro-Mechanical Systems (MEMS)*, ASME International Mechanical Engineering Congress and Exposition (Dallas), L. Lin, K. E. Goodson et al. (Eds.), ASME, Vol. DSC-234/HTD-354, pp. 47–53.